Currents on the northern shelf of the Yellow Sea

Fan Lin [a,b,d], Lars Asplin [c,*], W. Paul Budgell [c], Hao Wei [e], Jianguang Fang [a,b]

[a] *Yellow Sea Fisheries Research Institute, CAFS, Qingdao, China*
[b] *Laboratory for Marine Fisheries Science and Food Production Processes, Qingdao National Laboratory for Marine Science and Technology, China*
[c] *Institute of Marine Research, Norway*
[d] *Geophysical Institute, University of Bergen, Norway*
[e] *School of Marine Science and Technology, Tianjin University, Tianjin, China*

ARTICLE INFO

ABSTRACT

The currents of the northern shelf of the Yellow Sea are investigated using observations of current and hydrography and numerical current model results. The Regional Ocean Model System (ROMS) with a horizontal resolution about 1km is implemented for the Yellow Sea and the Bohai Sea, and the results are produced for the year 2014 and 2015. Observations from bottom moored ADCP profilers and CTD on the northern shelf of the Yellow Sea are used for validation of the model. The comparison of current time series and bottom temperature evolution show good agreement between model and observation. Barotropic tides are the dominant current component throughout the year on the shelf and consistently mixing the water column in the shallower parts. A thermal front and associated jet exists during the summer creating a robust current structure on the western part of the shelf. The winds in the region are changing constantly creating episodic currents in the upper part of the sea lasting from hours to a couple of days.

1. Introduction

This study aims at investigating the currents at the northern shelf of the Yellow Sea (YS). This refers to the coastal water south of the Liaodong Peninsula towards Korea Bay including the Zhangzidao Islands. The bottom depths are shallower than 40–50 m. This area has great importance for aquaculture of especially bottom cultured scallops (Mao et al., 2019). According to the Chinese Fishery Statistical Yearbook 2018, Liaoning province have produced about 472,230 metric tons of cultured scallops, which accounts for about 23% of the total domestic production. The bottom cultured scallops usually take about 3 years to grow up to market level, and recent frequent high scallop mortality within this region has drawn more attention for researchers to studies of ecology and carrying capacity (Zhao et al., 2019). Regarding the sustainable development of the scallop industry on the northern shelf of YS, the understanding of the physical environmental variation and the related driving forces will be crucial.

The Yellow Sea at large is relatively thoroughly investigated. As a semi-enclosed sea in the Western Pacific, surround by the mainland of China and the Korean peninsula, it covers an area of approximately 40,000 km^2 with an average depth of about 44 m (Wei et al., 2010). Recent overviews by Hwang et al. (2014) and Tak et al. (2016) illustrates the general forcing and responses of the water masses in the Yellow Sea. Other studies have illustrated the water masses, especially the Yellow Sea Bottom Cold Water, and general circulation (Li and Yuan, 1992; Su and Huang, 1995; Ichikawa and Beardsley, 2002; Xia et al., 2006; Wang et al., 2014; Zhu et al., 2018). The thermal fronts on the shelves are of particular interest, and is commented in e.g. Liang et al. (2018) and in studies illustrating that these can have a major effect on the phytoplankton growth and biological production (Chen, 2009; Li et al., 2006; Xin et al., 2015; Sun and Cho, 2010).

The conditions at the northern shelf have received less focus, although similarities with other shelf areas around the Yellow Sea are apparent. Zhuang et al. (2017) analyzed the tidal and mean current characteristics with moored current profiling data near Zhangzidao island during June-November in 2009. They found a barotropic diurnal and semi-diurnal tide at the observation location and that the summer stratification has an impact on the vertical structure of the residual currents. Qi et al. (2013) implemented a numerical current model based on FVCOM to simulate the tidal current on the northern shelf near Zhangzidao island. The model result and the observation have showed a major regular semi-diurnal pattern around the island with counter-clockwise rotated tidal current. The tidal residual current has been evaluated to be around 0.08–0.12 m/s around the islands and reduced to about 0.01–0.02 m/s further from the coast. Li and Zhai (2018) studied the subsurface-water pH and aragonite saturation from cruise data during 2011–2013, and identified the

---

contributions from various biogeochemical processes within the north YS cold water mass.

In our study, we focus on the most important current components acting on the northern shelf of the Yellow Sea. We use information from observations by current meters and CTD-sondes when available, although most information is from numerical current modeling and various model results archives. We show that the model results are in good agreement with the available observations. The tidal current is the most important current component in the area. The wind is creating a relatively high frequent current confined to the upper ∼10 m with periods or unidirectional flow being hours to a few days. A frontal jet associated with the temperature distribution on the shelf is apparent in late summer and capable of moving water of the same order of magnitude as the whole water mass of the western part of the shelf for that period.

2. Materials and methods

2.1. The current model

The regional Ocean Modeling System (ROMS) is a free surface, terrain following, primitive equations, hydrostatic ocean model on an Arakawa-C grid (Haidvogel et al., 2008; Shchepetkin and McWilliams, 2005). ROMS is widely used in coastal studies, e.g. along the Norwegian coast (Albretsen et al., 2012). Our implementation of the ROMS for the Yellow Sea is named the Yellow Sea Model (YSM). The YSM covers the Yellow Sea and Bohai Sea with the horizontal grid size being latitude by longitude (∼1 km), and there are 40 vertical layers derived with the stretching factors 7.0, 2.0 and a minimum depth of 15 m giving enhanced resolution near the surface and the bottom. The model grid is rotated counter-clockwise to have one open boundary towards the border between the Yellow Sea and the East China Sea. The model bathymetry is interpolated from SRTM30-plus shuttle radar altimetry supplemented with side-scan sonar survey data and the GEBCO 30" database (Becker et al., 2009) and smoothed with a low-pass filter (Fig. 1). The model is configured with 3rd-order upstream horizontal advection of tracers and 4th-order centered advection for momentum with the Generic Length Scale k-kl vertical mixing scheme (Warner et al., 2005).

Atmospheric forcing is obtained from the European Center for Medium-Range Weather Forecast ERA-Interim Reanalysis datasets (Dee et al., 2011), including 10 m wind velocity, surface specific humidity (derived from 2 m dew point temperature), surface air temperature (2 m), downward long wave and shortwave radiation, precipitation and mean sea level pressure. Accumulated data such as radiation and precipitation are 12-hourly data with spatial resolution of 0.75°, and the rest are 6-hourly data at spatial resolution of 0.25°. Atmospheric forcing is interpolated to the model grid, and the net heat flux is computed from a bulk formulae by Fairall et al. (1996).

Open boundary data includes tide, daily mean elevations, daily mean vertical momentums, temperature and salinity. The mean values are obtained from the HYCOM daily global ocean reanalysis and were interpolated to the YSM grid. Eleven tidal components (M2, K2, S2, N2, K1, P1, O1, Q1, MN4, M4 and MS4) from the Oregon State University global inverse tidal model of TPXO7.2 (Egbert and Erofeeva, 2002) were specified at the open boundary. Open boundary data are imposed with a radiative-nudging scheme and a quadratic bottom drag was employed with the friction coefficient of 0.0025 applied to the entire model domain.

The model was run for 29 months from August 2013 to December 2015. The initial conditions were interpolated from the HYCOM reanalysis mentioned above. Model results were stored as hourly and daily mean values and are validated against the observed current and temperature.

2.2. The observations

Observations include *in-situ* measurement of current and hydrography. A Nortek ADCP Aquadopp Profiler (1.0 MHz, bin size 1.0 m, 20 bins) was moored at the bottom near the Zhangzidao Island. The accuracy of the instrument is 1% measured value +/−0.5 cm/s for current profiling, +/−0.1 for the integrated temperature sensor and 0.5% of maximum range for the pressure sensor. The instrument was deployed twice at different periods and different locations in 2015 (Fig. 1). First deployment was from March to April and the second from September to December. The instrument was moored at the sea floor and measuring upwards with a range of approximately 20 m. Instrument depths were 52 m in the first period (ADCP A) and 39 m in the latter (ADCP B). The bottom temperature and pressure time series were recorded with integrated sensors.

On July 8th, 2015, nine stations of vertical temperature profiles were measured with a Seabird SBE 19plus V2 profiler CTD. Geographical locations of the measurement sites are shown in Fig. 1. The initial accuracy the CTD is 0.005 for temperature and 0.1% full scale range for pressure sensor.

3. Results

The total current at a location will be assembled as a sum of current components from specific forcing agents plus potentially some non-linear contributions. Usually it is meaningful to analyze currents based on individual components created by the separate forcing mechanisms like tide and wind etc., which is what we do in the following.

3.1. The tidal current

The tidal current at the northern shelf is strong with an amplitude in surface elevation of around 2 m. A number of tidal constituents are identified as active, but the main is the semidiurnal M2 component from the moon. A total of 11 constituents are included at the open boundary of the numerical model simulation.

Horizontal current components from the current meter locations near the Zhangzidao island (ADCP A and B) at approximately 10 m above the bottom show a good agreement between observed and modeled current (Fig. 2) with values varying between +/−0.4–0.6 m/s. The correlation coefficient for the modeled and observed u and v component at ADCP A and ADCP B are 0.92, 0.96, 0.94 and 0.97 respectively. The corresponding root-mean-square errors are 0.08 m/s, 0.07 m/s, 0.07 m/s and 0.10 m/s for each component. The largest root-mean-square error for the presented time series is about 19% of the observation maximum value. In general, the numerical model results resemble the observations realistically. The velocity basically follows the spring–neap cycle of the tidal period. The maximum current magnitude is larger at ADCP B, i.e. at a shallower depth closer to the coast. In the model, the u component is slightly underestimated and the v component, on the contrary, is slightly overestimated.

The tidal ellipses extracted from time series of the numerical model results illustrates a variety of eccentricities, from high (flat) to low (circular), typically determined by the topography (Fig. 3). In areas near islands and the coast the tidal motion will be more back and forth, while at the open shelf the tidal ellipses are less eccentric.

If we compute the tidal ellipse from the M_2 constituent horizontal flow in the vertical, we will discover any baroclinicity. A baroclinic tidal signal will be possible if the water column is stratified, and we will present results from three locations T1–T3 (Fig. 1) where T1 is offshore and in a stratified water mass, T2
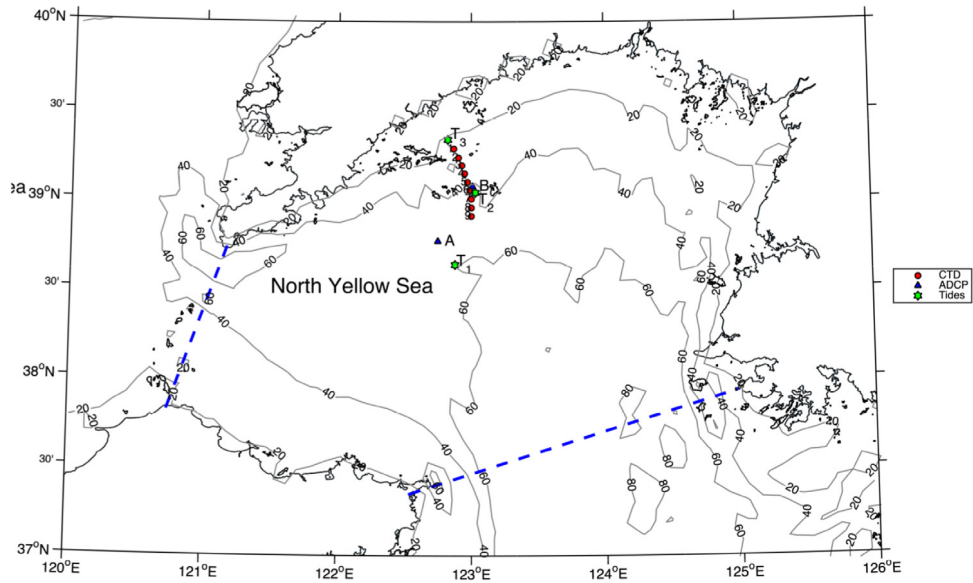
Fig. 1. The northern shelf of the Yellow Sea and the locations of the observations (blue triangles for current observations, red dots for ctd profiles) and the locations for extraction of vertical tidal ellipses (green stars). (For interpretation of the references to color in this figure legend, the reader is referred to the web version of this article.)
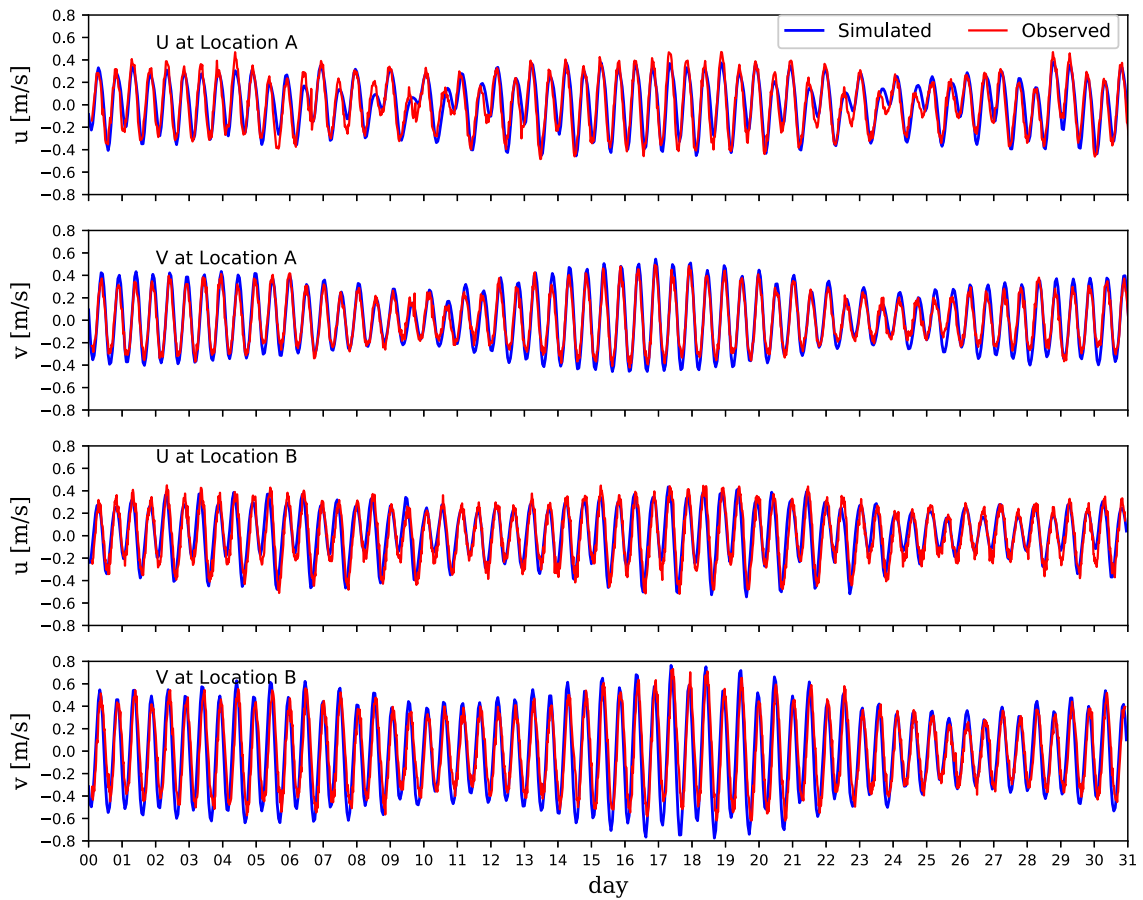

Fig. 2. Observed (red line) and modeled (blue line) current components (m/s) at the locations ADCP A (March 2015) and ADCP B (October 2015).. (For interpretation of the references to color in this figure legend, the reader is referred to the web version of this article.)

is weakly stratified and T3 nearly homogeneous. We will show results from both summer season and winter season, where the latter represents homogeneous water at all three locations. The

stratification is mainly due to vertical variation of water temperature (Fig. 4). The tidal ellipses show little vertical variation for the two innermost locations T2 and T3 both in winter and
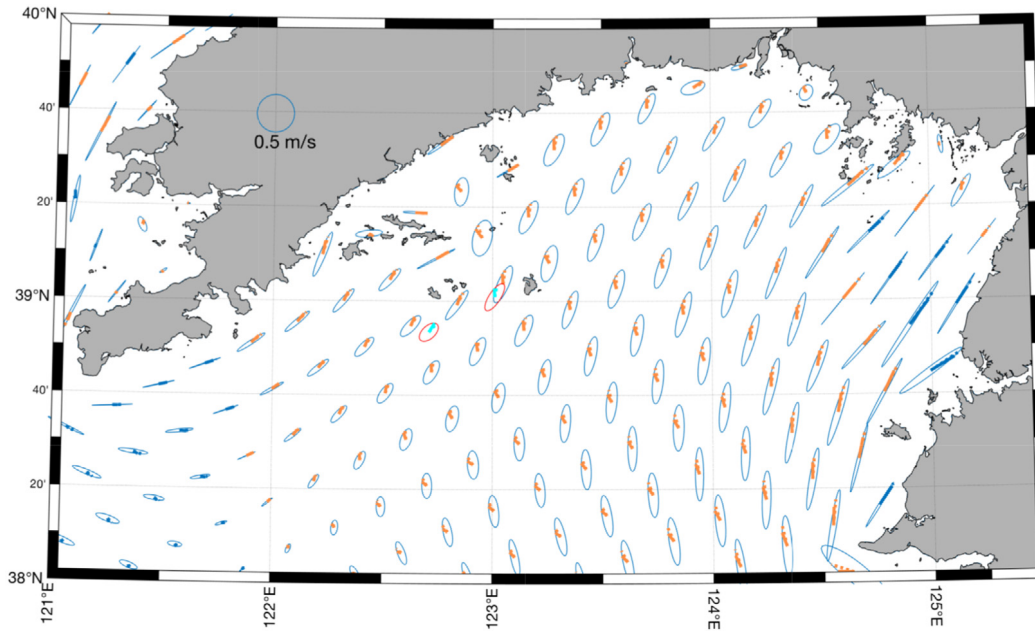
Fig. 3. Tidal ellipses on the northern shelf of the Yellow Sea for the M$_2$ constituent from the numerical model results. The arrow inside the ellipses indicate current direction for the same phase (red color indicates anticyclonic rotation, blue color cyclonic rotation). The tidal ellipses derived from depth averaged observed velocity is shown in red for the two current meter locations ADCP A and B near the Zangzidao islands. (For interpretation of the references to color in this figure legend, the reader is referred to the web version of this article.)

summer, while at the offshore location T1 there is a reduction in the upper 10–20 m during summer when there is a two layered water column. For all locations there is a reduction of ellipse size towards the bottom due to bottom friction.

3.2. Seasonality of water temperature and the thermal front jet

Observations and numerical model results from the locations of ADCP A and B (locations shown in Fig. 1) illustrate the annual cycle of water temperature at a single point (Fig. 5). Minimum water temperature appears in the early spring and maximum in late autumn. At these locations the minimum value is around 3–4 °C and maximum around 18–20 °C. The observed water temperature is in agreement with the numerical model results with a correlation coefficient and root-mean-square error of 0.96 and 0.27 °C at ADCP A and 0.98 and 0.40 °C at ADCP B. Closer to the coast, the maximum summer bottom temperature and minimum winter bottom temperature from the model results are above 25 °C and less that −1.5 °C respectively, indicating a large interannual difference.

To illustrate the warming of the shelf water through the summer season, numerical model results of bottom water temperature are extracted for the days May 1, June 1, July 1, August 1, September 1 and October 1 (Fig. 6). In May most of the bottom water is cold and less than 6–8 °C but the beginning of a warming is seen near the coast. One month later, the water temperature at the shelf has increased to around 15 °C for most areas shallower than 30 m. Such an increase continues through the summer and early autumn, but restricted to depths shallower than ~40 m at least for the western part of the shelf. In October the bottom water temperature has started to decrease after a maximum in September.

From a vertical section of temperature observation at June 8. 2015 (location in Fig. 1) a thermal front is found around the locations of the 30–40 m isobaths (Fig. 7). The upper warm layer is about 15 m deep and relatively homogeneous with at temperature just above 20 °C. The thermocline of the numerical model is shallower and only ~5–10 m, but the structure of the

surface and bottom thermal front is similar between the two results, as well as the location of the fronts at around the 30–40 m isobaths.

Observations of salinity from the same vertical section indicated little vertical variations and values around 32. The quality of the observations turned out to be poor with much noise, and values are not presented.

Monthly mean values from our numerical model results of current at 20 m depth illustrate the evolution of a frontal jet system along the shelf (Fig. 8). The strongest flow appears in August and September with an almost continuous jet from the longitude of 123 °E extending about 200 km westward to the tip of the Liaoning Peninsula.

A closer look on the vertical structure of the jet along a cross section stretching south-south east offshore starting at 122 °E for August 25th, 2015 shows a strong bottom thermal front, a weaker surface front and a jet flowing westward (into the page, negative values) extending vertically down to 30–40 m depth (Fig. 9). The width of the jet is ~40 km but the core is only ~20 km wide. The internal radius of deformation at this latitude and based on the present vertical density stratification is ~5 km. The jet does not extend all the way to the bottom, although the iso-therms are forming a distinct bottom front.

3.3. Wind driven current

Calculating mean winds for 2014 and 2015 for the two seasons extracted from the ERA archive we find that the summer circulation and winter circulation differ with southerly and relatively weak mean wind in the months May to August and stronger northerly mean wind during September to April (Fig. 10).

The wind driven currents are created by wind episodes of shorter duration, and to examine this we have extracted a time series of the wind component in the North-South direction approximately at the location of the ADCP A current meter at the southern part of the shelf (Fig. 11). The values are from January 2011 until March 2016 and are based on 3 hourly winds from the
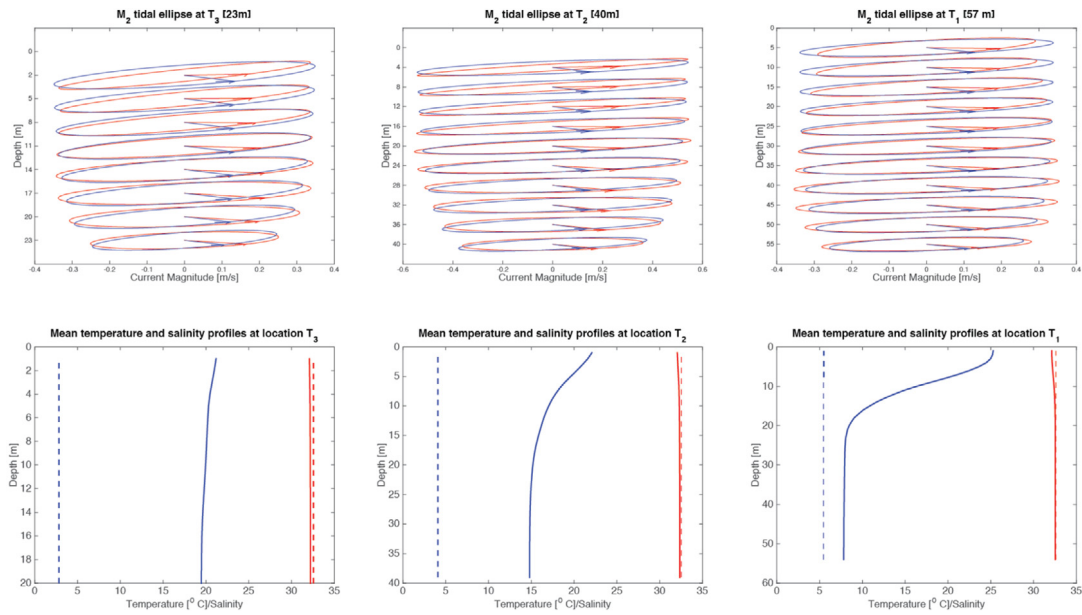
Fig. 4. Vertical distribution of tidal ellipses from the M_2 constituent horizontal flow for three locations T1, T2 and T3 (locations shown in Fig. 1) with corresponding vertical temperature (°C) and salinity profiles in the lower panels. In the upper panels the red color illustrate results for the summer period and blue results for the winter period. In the lower panels, solid lines are results for the summer period and dashed lines results for the winter period. (For interpretation of the references to color in this figure legend, the reader is referred to the web version of this article.)
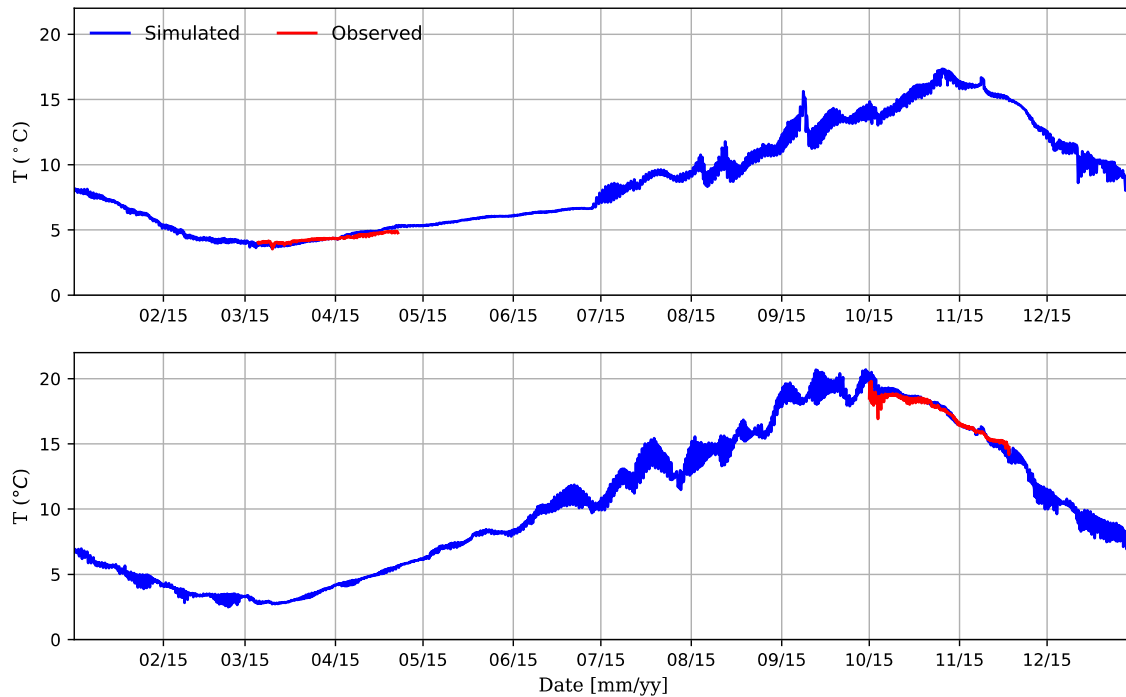

Fig. 5. Water temperature (°C) near the bottom at the location ADCP A (top) and ADCP B (bottom) for January to December 2015. The blue line represents the numerical model results while the red line is observations by the current meter. (For interpretation of the references to color in this figure legend, the reader is referred to the web version of this article.)

Table 1
Values from the ERA-Interim atmospheric archive at the ADCP A location of the north–south component of the wind at 10 m height.

	Episodes	Mean duration	Max duration	Mean speed	Max speed
Northerly	175	13 h	60 h	5.1 m/s	19.2 m/s
Southerly	28	8 h	30 h	3.7 m/s	12.7 m/s

ERA archive. The seasonality with southerly winds during summer (positive NS component) and northerly during the winter is apparent. Maximum values are above 10 m/s in both directions. There are not many periods of calm winds, but an on-going
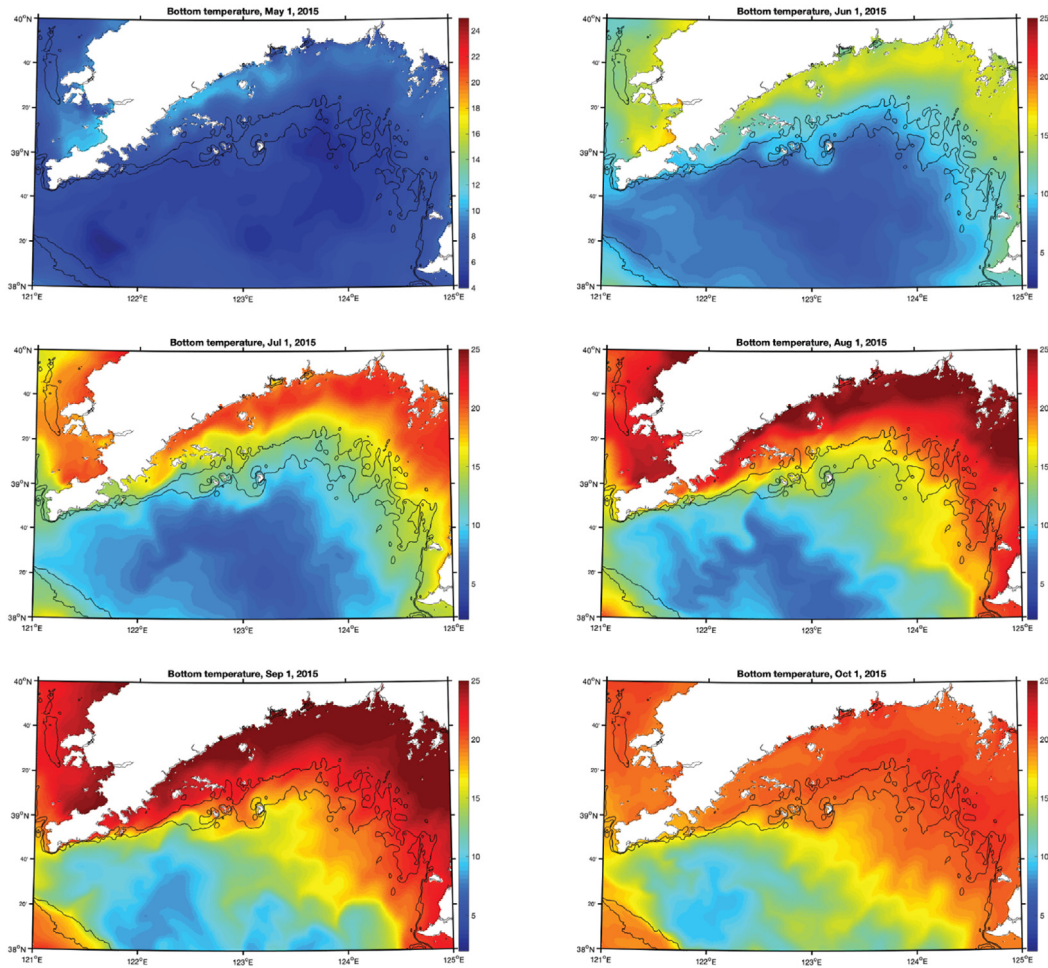
Fig. 6. Evolution of the bottom temperature (°C) between May 1 and Oct 1, 2015, from model results. The contour lines of 30 and 40 m depths are shown.
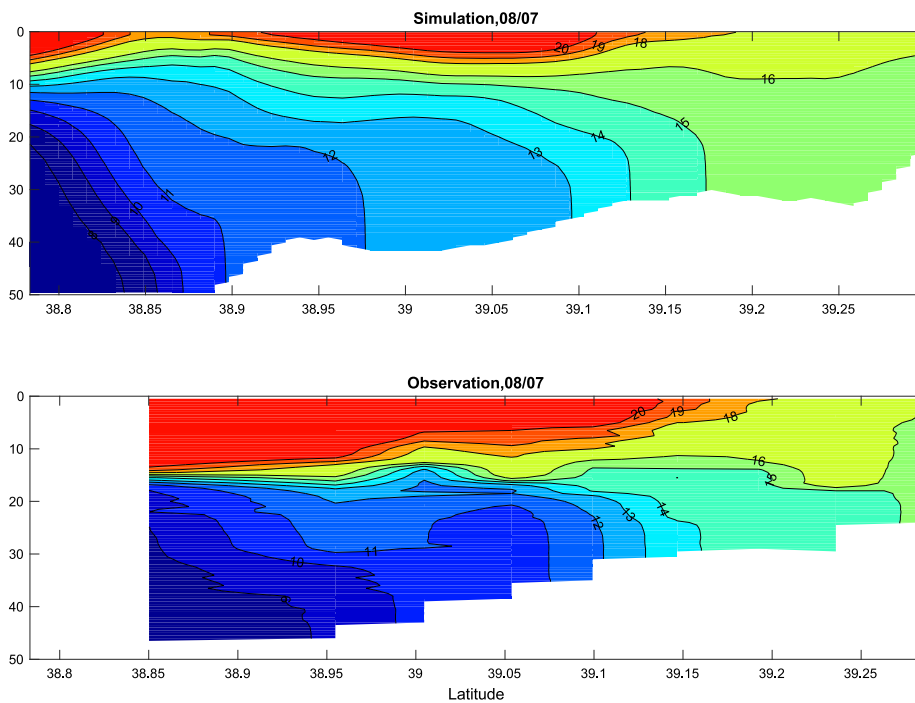

Fig. 7. Along section of temperature (°C) on June 8, 2015, from the numerical model results (top) and observations (bottom).
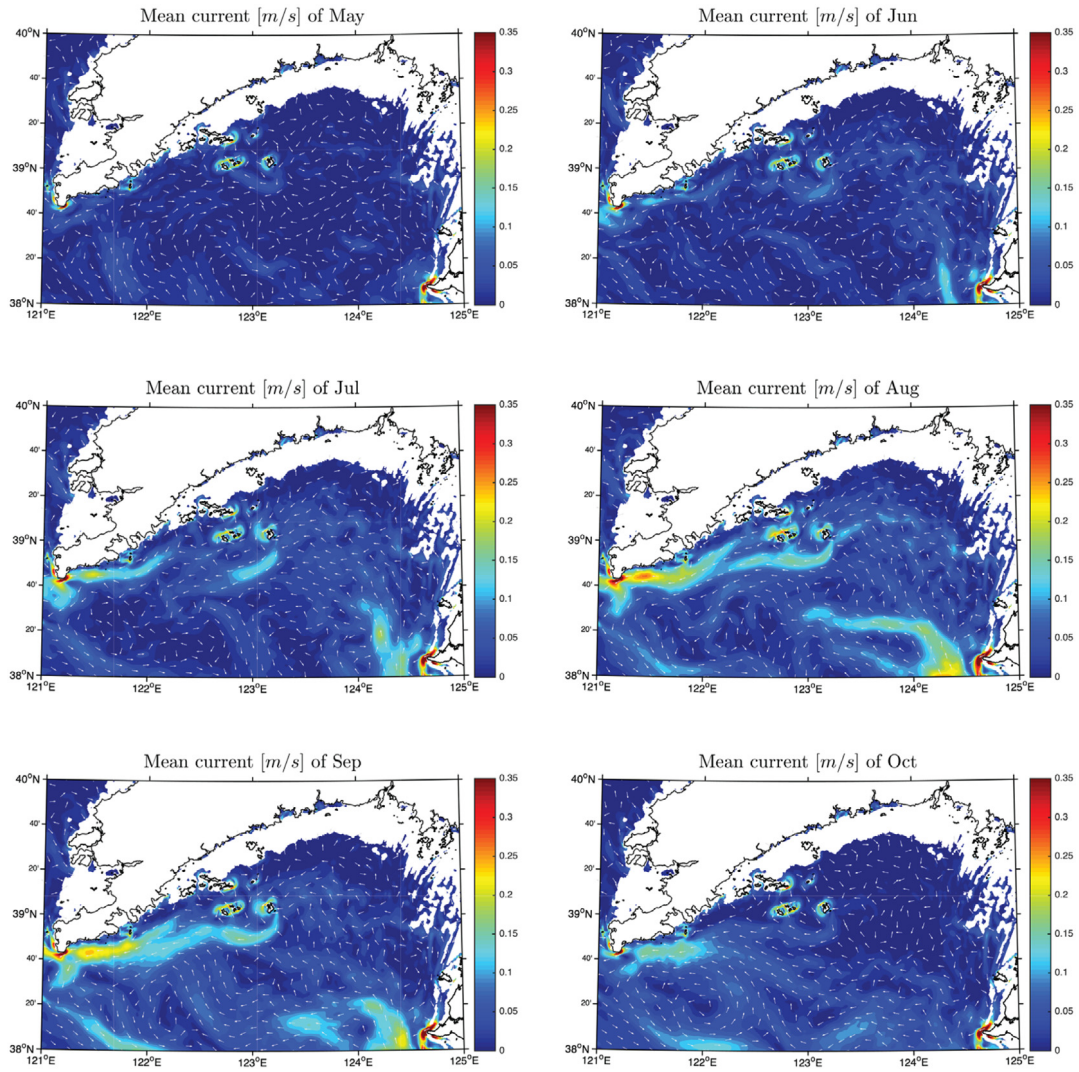
Fig. 8. Monthly mean current (m/s) at 20 m depth from the numerical model results for May to October, 2015.
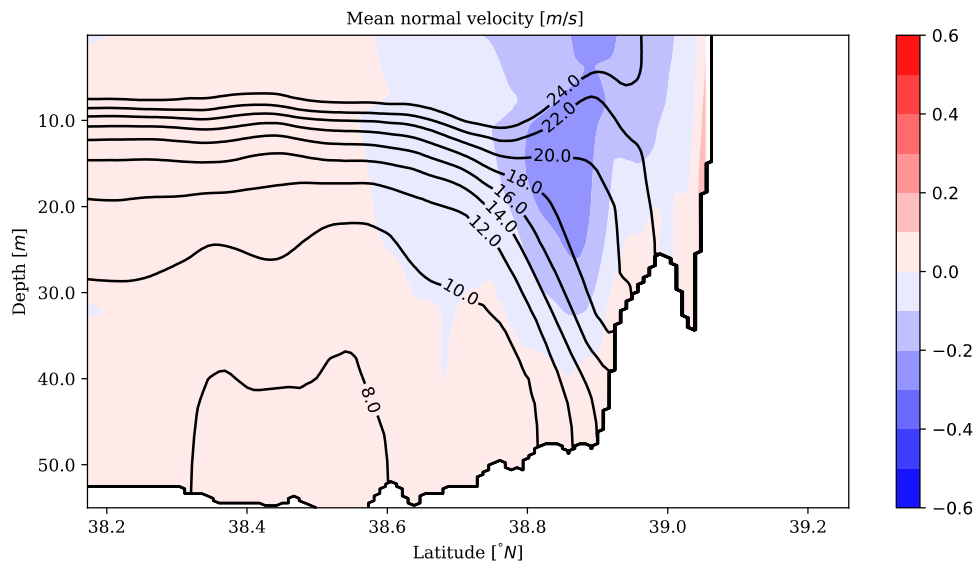

Fig. 9. Vertical view of the daily mean velocity (color) across the section and the temperature (contours) along the section on August 25th, 2015. (For interpretation of the references to color in this figure legend, the reader is referred to the web version of this article.)
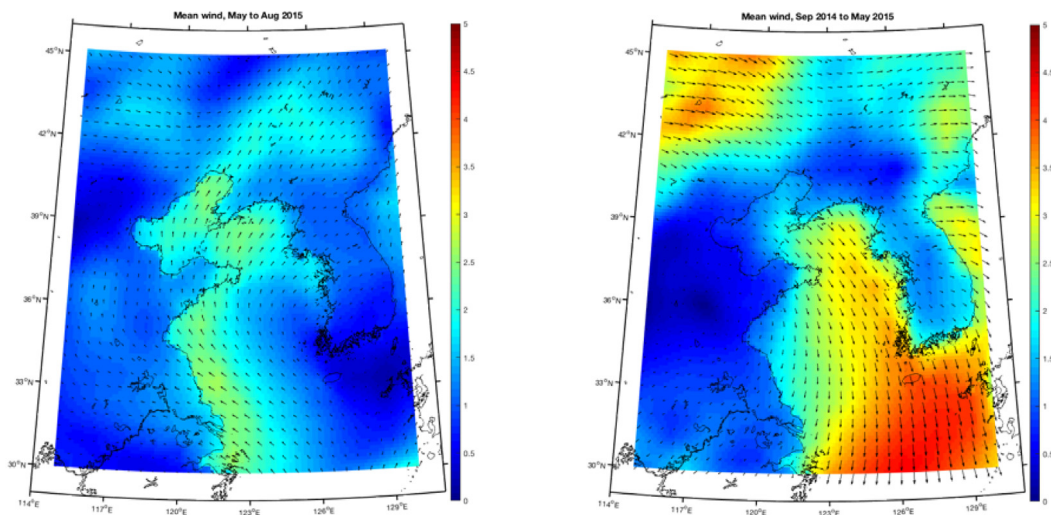
Fig. 10. Mean winds (m/s) for the summer period (left) and the winter (right) extracted from the ERA-Interim 3 hourly wind archive.
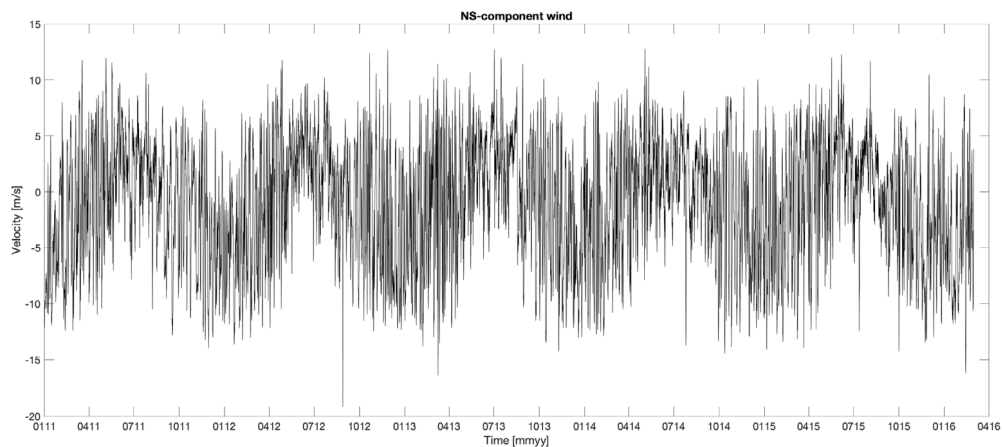

Fig. 11. North-South component of wind (m/s) at 10 m from the ERA-Interim archive at the location of the ADCP A current meter.

fluctuation of episodes. Maximum wind speeds are moderate and never reaching a value to be classified as a storm.

If we count the duration of the episodes with absolute wind value larger than 10 m/s, we find that this occur about 7 times more frequent for winds from the north (winter) than from the south (summer) (Table 1). Northerly winds with speed larger than 10 m/s occur 175 times during the ∼5 years period and the mean duration of such episodes is 13 h and maximum duration 60 h. This indicates such an episode almost weekly. The similar numbers for winds from south are 28 episodes, lasting on average 8 h and with maximum duration of an episode being 30 h.

To illustrate the effect of a wind episode on the current, we choose a situation from March 31, 2015, when there was a northerly wind lasting for ∼20 h. The situation on March 31 at 12 o'clock shows a northerly wind covering the northern part of the Yellow Sea and even stronger in the Bohai Sea (Fig. 12). The corresponding surface current after a 24 h lowpass filter (4th order Butterworth) has been used to remove the main tide, is westward and with speed between 0.1 and 0.2 m/s with higher values towards the west on the shelf (Fig. 13).

If we look at a time series of the surface current components at the location of the ADCP A current meter between March 30 and April 3, 2015, we find that the east–west current component on March 31 adds on to the tide to create a surface current of more than 0.4 m/s (Fig. 14). The 24 h lowpassed current component, mainly consisting of the wind driven part, is westward with

a maximum current speed of ∼0.17 m/s. On April 2 the wind direction changes to more southerly, and another episode with current towards north-east is created. Later the same day and the next, a southerly current is apparent again. The absolute value of the lowpassed surface current has a maximum of around 0.2 m/s.

The vertical profile of lowpass filtered current speed illustrates the vertical extension of the wind driven flow component (Fig. 15). For the three times where we have identified different wind episodes, i.e. March 31, April 2 and April 3, 2015, the current speed has maximum around 0.2 m/s at the surface and is rapidly decreasing downwards to approximately 20 m depth.

3.4. Particle dispersion

In order to illustrate the water mass transport capacity of the different current components, a simple particle dispersion calculation has been performed. We have chosen four time periods where two periods consist of mainly wind driven flow component, one period with mainly tidal flow component and one period with the thermal front jet component. Particles are seeded one in each grid square and advected with the current without additional dispersion. We use 121 particles and let them drift horizontally for 25 h (Fig. 16). For the wind driven flow experiments, March 31 and April 1, 2015 are used, and we use 24 h lowpassed current. In the first period the particles drift initially to the west and then to the north. The net movement
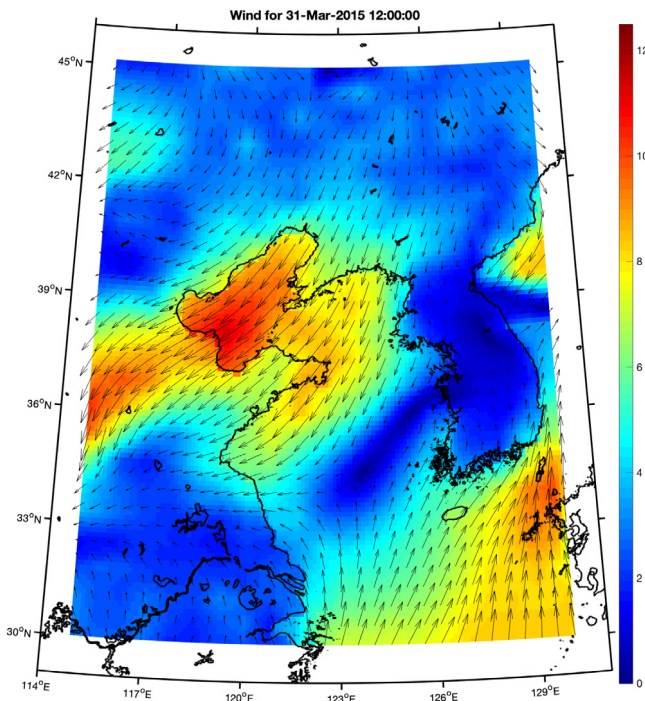
Fig. 12. Wind (m/s) at 10 m height from the ERA-Interim archive on March 31. 2015, at 12 h.

of the particles are 5–10 km in 25 h. Particles seeded on April 1 are subject to a current generated by a northerly wind, and will drift towards the south and with a net dispersion distance also of 5–10 km. The third period illustrates the particle dispersion by the tidal flow, and we subtracted the 24 h lowpassed current from the total current with the main tidal flow remaining. We have also chosen a period with a relatively strong tidal flow with current amplitude of approximately 0.5 m/s. During the 25 h drift, the net movement of the particles are modest while the total drift is much larger with the maximum distance of the particles away from the initial location being 5–10 km. For the dispersion of the

particles by the thermal front jet, we have chosen September 1–2, 2015, and the 24 h lowpassed filtered current at 20 m depth. The particle dispersion for those captured in the relatively narrow jet is stable towards the west, and after 48 h around 30 km is covered.

4. Validation of the numerical model results

Numerical current model results validation is an exercise that should be as extensive as possible and also one that never ends (Dee, 1995). A numerical current model might perform good while standard statistical error metrics as root-mean-square or cross-correlation still can be large (Ziegeler et al., 2012). The Yellow Sea Model is implemented from the ROMS current model which has been extensively applied for coastal seas worldwide, e.g. the NorKyst800 model system for the Norwegian coast (Albretsen et al., 2012) or TFOR for the Taiwan Strait (Xinyou et al., 2016). These implementations has proven to produce realistic results and useful applications (Asplin et al., 2013; Johnsen et al., 2014; Sandvik et al., 2016; Xinyou et al., 2016).

The horizontal current speed at 10 m above the bottom is in good agreement with the independent observations (least correlation coefficient is 0.92 and largest rms error is 0.10 m/s). The 20 m measurement range of the ADCP limits the observations to the lower part of the water column, where the tidal flow is dominating. Potential erroneous bathymetry in the model can be responsible for the small deviations in both modeled elevations and currents compared to the observations. Improving the bottom depth in the model domain will be important when developing the model further.

Model results of temperature distribution resembles the observations in both variability on longer and shorter time scales. For the temporal development of temperature measured by the current meters (Fig. 5), the least correlation coefficient is 0.96 and the largest root-mean-square error is about 0.40 °C.

We find that the numerical model underestimates the mixed surface layer (Fig. 7), which is previously reported for the ROMS model and the GLS turbulence formulation (Robertson and Hartlipp, 2017). To simulate the mixing of the upper layer water masses and the sharp transitions is generally challenging for numerical models. The action of surface waves, which is not included in the model, might also represent a mixing agent of
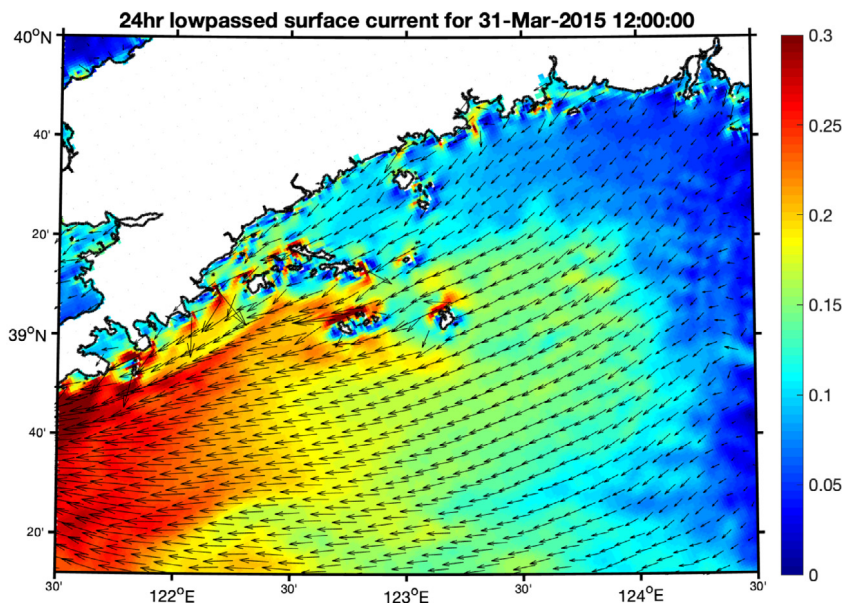

Fig. 13. 24 h low-pass filtered surface current (m/s) from the numerical model results on March 31, 2015 at 12 h.
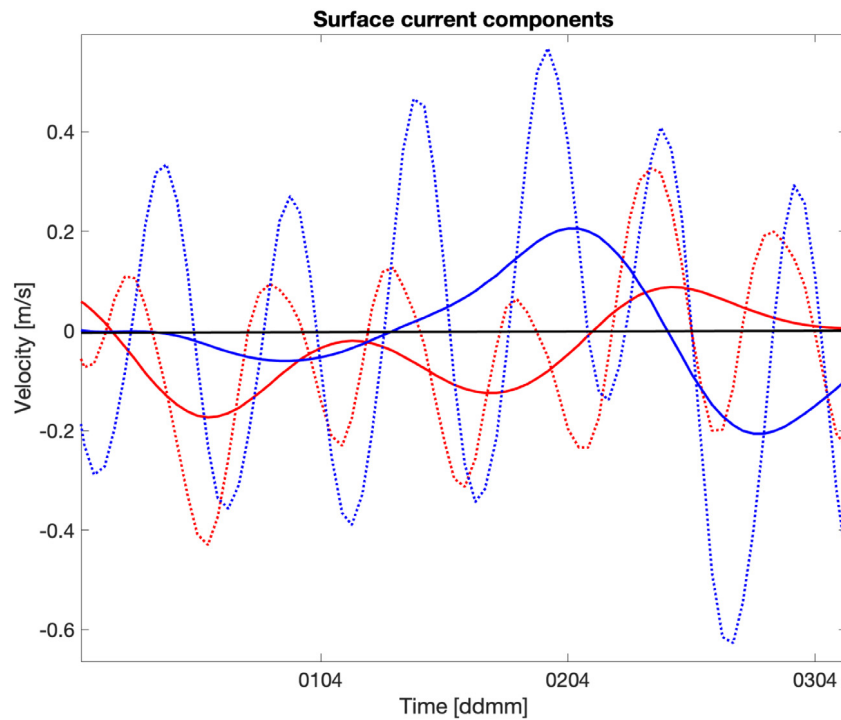
Surface current components

Fig. 14. Time series of the components of the surface current (m/s; EW = red lines, NS = blue lines) at the location of ADCP A from the numerical model results between March 30 and April 3, 2015. Solid lines show the 24 h low-passed values. (For interpretation of the references to color in this figure legend, the reader is referred to the web version of this article.)
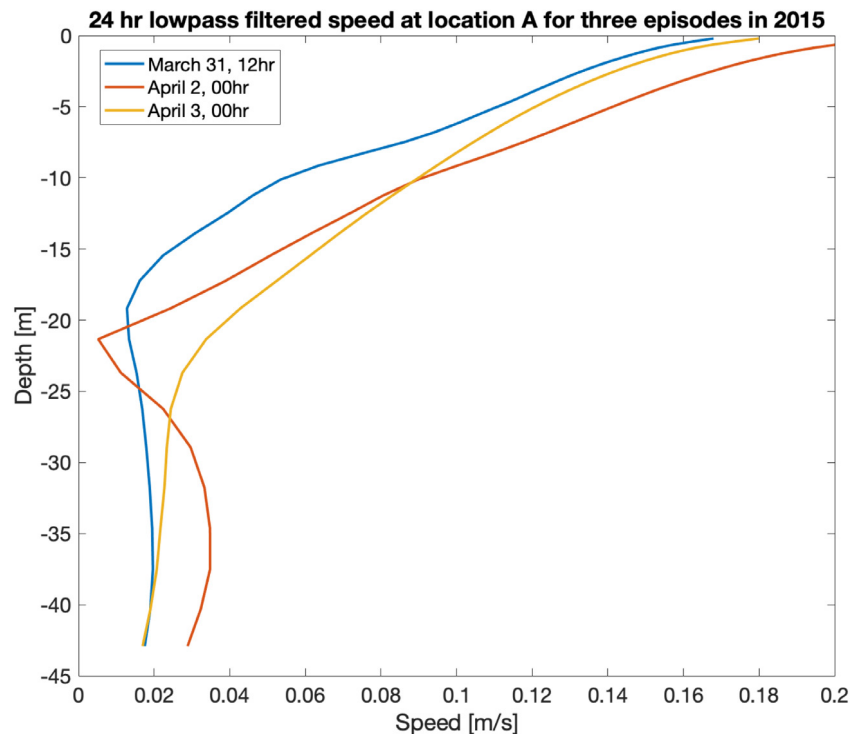
24 hr lowpass filtered speed at location A for three episodes in 2015

Fig. 15. Vertical profile of 24 h lowpassed current speed (m/s) for three time periods at the location of ADCP A.

importance and one possible explanation of an underestimated mixed layer depth. Still in spite of a slightly misplaced thermocline, the frontal structure and the lateral position of the bottom and surface fronts are reasonably reproduced (Fig. 7).

An advantage with numerical model results is the huge temporal and spatial information provided. The more details included

in the model results, the more likely is a small offset in time and space. Since all motion in the ocean is assembled by numerous waves with potentially different phase velocities and amplitudes, as well as an in principle chaotic sub-grid scale turbulent motion, small errors in the numerical simulation and parameterization of these can lead to small displacements, typically as seen in
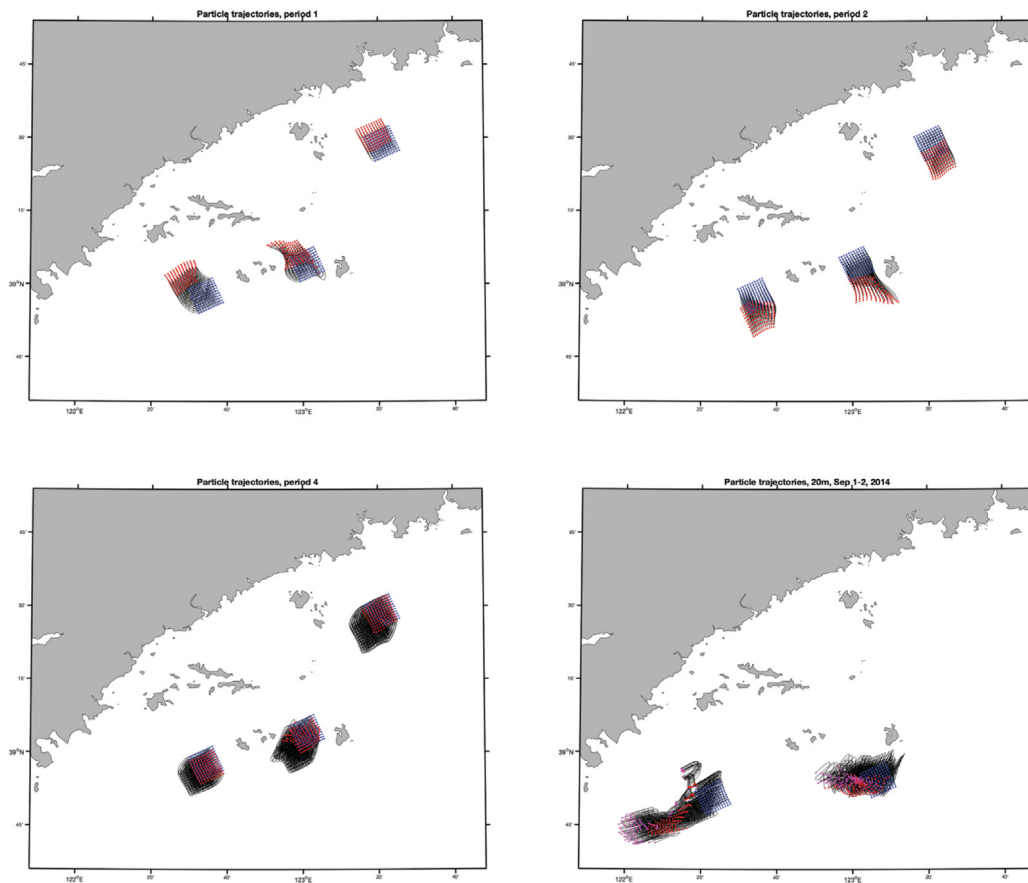
Fig. 16. Trajectories of particles dispersed in the horizontal current at four different episodes. Upper left panel shows 25 h drift on April 1, 2015, with a south-easterly wind episode dominating the lowpassed surface current. Upper right panel shows 25 h of drift om April 2, 2015, and a northerly wind episode. Lower left panel shows trajectories of 25 h drift using the tidal current during a spring tide period and lower right panel shows trajectories from 25 and 48 h drift of particles at 20 m depth on September 1–2, 2015, using 24 h lowpassed current illustrating the effect of the thermal front jet on dispersion. The blue dots represent the initial particle location and the red dots the locations after 25 h drift. The magenta dots represents locations after 48 h drift. (For interpretation of the references to color in this figure legend, the reader is referred to the web version of this article.)

the present comparison between the model results and the observations. Overall, we find that the numerical model delivers a reasonably adequate set of results resembling the same variability as the available observations, and the results will prove useful as information to explore the dynamics and the ecosystems of the Yellow Sea.

5. Discussion

The Yellow Sea is of great ecological importance for marine fishery and the huge aquaculture along its coast, and the northern shelf is an important area for scallop aquaculture (Mao et al., 2019). To understand variability of both natural and farmed ecosystems, it is crucial to understand the variability of the environmental conditions. Water temperature determine the physiology of living organisms and water current determine food availability, water exchange and potential dispersion of diseases. We have investigated the currents of the northern shelf of the Yellow Sea using mainly results from a current model with additional information from a few observations. The observations are a necessary supplement to validate the model results while the latter give us a sufficient information to understand the huge spatial and temporal variability going on.

The tidal current is strong and the dominating current component in the area. The semi-diurnal component is the strongest, meaning the flow will be high frequent and unidirectional for less than 6 h at a time. We find the tidal current to be mostly

barotropic, but in the stratified deeper parts there is a minor change of the size of the ellipses vertically (Fig. 4).

We are satisfied with the fact that the model results by and large resembles the observed tides, including the sea surface height (results not shown) since this current component supplies most of the energy to the area.

Around the islands in the western part of the shelf, there will be strong influence on the tidal current from the topography (Qi et al., 2013), but our numerical model set up with 1 km grid resolution is not designed to fully confirm this although our model results (not shown) have an intensified circulation around these islands.

The thermal front jet is a seasonal current system occurring only in the late summer (Fig. 8). The mechanism is similar to what described by Simpson and Hunter (1974) and Simpson (1981) from the Irish Sea, where the surface buoyancy input and the tidal mixing is controlling the water column structure with a front being established at a critical bottom depth. From studies at the northwest European shelf, Hill et al. (2008) found a thermal-wind, geostrophically balanced jet along the front. Xia et al. (2006), Shi et al. (2016) and Liang et al. (2018) showed similar frontal jets on shelf areas in the Yellow Sea, and our results agree with these reports.

Being forced by a thermal wind relation at the thermal front, the front jet is a persistent feature and a geostrophic balance is a preferred state of the nature and the way to spend the minimum energy (Gill, 1982). This current will be limited to the area of the

thermal front though, extending only 20–40 km across (Fig. 9). The shelf area inside of the thermal front, e.g. where the water column is vertically mixed, is not directly affected by this current. The strong tidal current moves the whole shelf water mass back and forth within mainly the M_2 tidal period ($\sim$12.4 h) including the front. However, this movement will mainly be along the front in the area where it is at the strongest, i.e. south-west of the Zangzidao islands (Fig. 3).

The vertical temperature structure of the water column reveals both a surface temperature front and a bottom front similar to what is reported from the northwest European shelf (Hill et al., 2008). They especially highlighted the importance of the bottom temperature front, and on the northern shelf of the Yellow Sea with an extensive bottom aquaculture of e.g. scallops, water temperature and its variations will affect the organism growth. Thus, a precise description of such temperature variations is important in ecosystem models.

We expect the thermal front to be affected by various instability mechanisms, forced by tide, wind or surface heat flux (e.g. Wu et al., 2018). Such instabilities, waves or meandering is beyond the scope for the present work.

The wind driven current will be strongest at the surface and have a logarithmic (i.e. rapid) decrease towards the depth. The duration and strength of the winds determine the strength of the current. Vertically the wind driven current is limited as shown by the classical Ekman theory (Ekman, 1905) with the magnitude of the vertical turbulence coefficient determining the limiting Ekman depth. Typically an Ekman depth is in the range 10–30 m (e.g. Pollard et al., 1973; Madsen, 1977; Stigebrandt, 1985; Lentz, 1992) but the uncertainty is due to the generally unknown turbulence structure. Our model results seems to represent a vertical current structure as anticipated from theory and previous reports (Fig. 15). It is worthwhile to note that a proper description of the strong current shear in the upper few meters require a sufficient number of vertical coordinates, and that the wind driven current component will not directly affect the flow on the deeper parts of the shelf.

The ERA interim atmospheric archive resemble the large-scale atmospheric system in the Yellow Sea area as part of the East Asian monsoon system described in e.g. Hwang et al. (2014). The winds from the ERA-Interim archive reveal conditions on the Northern shelf that are variable, almost always windy and with a strong seasonality, but still with sufficient short time variability that wind driven current episodes of relatively uniform direction will be lasting for only hours to days before changing. Thus, the variability of the wind driven flow is almost on the same periodicity as the tide or slightly longer, and we find that the wind driven flow component in one directions typically is replaced by a similar flow episode hours to a few days later.

The current of the northern shelf of the Yellow Sea is determining the residence time of the water masses. How long the water resides in an area will be important for many reasons, e.g. to determine food availability for bottom cultured scallops, to estimate dispersion of water borne diseases or dilution of pollutants etc. The tide will move and stir water within a radius of 5–10 km (Fig. 16). Thus the tide is less important as a long distance transportations mechanism, but excellent for local transportation and very reliable as a stirring or mixing agent. Similar advection distances for the upper layer water masses due to the wind is also the case, mostly since the winds are not very persistent and rather fluctuate on times from hours to a few days. The thermal front jet on the other hand, is a persistent current and potentially capable of transporting water off the shelf towards the west. This current appears only in late summer so the gross effect might still be limited although seasonally important. With a monthly mean current speed of 0.10–0.15 m/s and the

width of the jet being 20–40 km, the capacity of transporting water westward from the shelf is apparent. As an example we consider the shelf area from Dalian and 100 km eastward and 40 km offshore and the upper 30 m of the water column. This volume consist of about 10^{11} m^3 of water. Assuming the thermal front jet to be 20 km wide, 25 m deep and have a mean current speed westward of 0.1 m/s for August and September, the volume transported by this current is also about 10^{11} m^3. Theoretically the thermal jet is then capable of flushing the whole western part of the shelf in the late summer months.

Climate change is an important issue, and the future climate will change also in the Yellow Sea. Parameters like the wind, precipitation/river runoff and temperature might be altered (IPCC, 2014). The various current components on the northern shelf of the Yellow Sea could indirectly be affected, and especially the wind driven current in the case that the atmospheric wind fields change. The tidal current will be unaltered in a climate change, thus the most important current component on the shelf will be less affected. A warming of the water will be on a long spatial scale, but the vertical stratification might change to a warmer surface layer and larger vertical gradient than today. The thermal front will probably remain at the same locations or at a slightly shallower depth contour if the energy needed to vertically mix the water column increases. The speed of the thermal front jet might also alter slightly. However, without any further studies, which apparently should be made, we cannot see now that a possible future climate change will affect the currents dramatically in this area.

6. Concluding remarks

We have implemented a high-resolution current model of the Yellow Sea based on the ROMS model and with an extensive set of forcing and open boundary conditions. The model results compare well with the available observations and we are confident that the information provided by the model will be useful for particularly supplying information of the physical environment to ecological studies.

Although we are satisfied with the model performance per se, improvements should be sought producing even better results. One obvious way to improve the performance is to have a better bottom topography. Usually the forcing of the model is a critical factor for performance, and potentially atmospheric forcing of higher spatial resolution and possibly more precise radiation balance might also improve the results. Testing of internal model constructions as turbulence sub-models (which ROMS has a number to choose from) and the arrangement of the vertical grid, can also make the model perform better. A dynamical coupling to a specific surface wave model will also potentially improve the simulation of the surface mixed layer.

References

Albretsen, J., Aure, J., Sætre, R., Danielssen, D.S., 2012. Climatic variability in the Skagerrak and coastal waters of Norway. ICES J. Mar. Sci. 69 (5), 758–763.

Asplin, L., Johnsen, I.A., Sandvik, A.D., Albretsen, J., Sundfjord, V., Aure, J., Boxaspen, K.K., 2013. Dispersion of salmon lice in the Hardangerfjord. Mar. Biol. Res. 10, 216–225. http://dx.doi.org/10.1080/17451000.2013.810755.

Becker, J.J., Sandwell, D.T., Smith, W.H.F., Braud, J., Binder, B., Depner, J.L., et al., 2009. Global bathymetry and elevation data at 30 arc seconds resolution: SRTM30_PLUS. Mar. Geod. 32 (4), 355–371.

Chen, C.T.A., 2009. Chemical and physical fronts in the Bohai, Yellow and East China seas. J. Mar. Syst. 78 (3), 394–410.

Dee, D.P., 1995. On-line estimation of error covariance parameters for atmospheric data assimilation. Mon. Weather Rev. 123 (4), 1128–1145.

Dee, D.P., Uppala, S.M., Simmons, A.J., Berrisford, P., Poli, P., Kobayashi, S., et al., 2011. The ERA-interim reanalysis: Configuration and performance of the data assimilation system. Q. J. R. Meteorol. Soc. 137 (656), 553–597.

Egbert, G.D., Erofeeva, S.Y., 2002. Efficient inverse modeling of barotropic ocean tides. J. Atmos. Ocean. Technol. 19 (2), 183–204.

Fairall, C.W., Bradley, E.F., Rogers, D.P., Edson, J.B., Young, G.S., 1996. Bulk parameterization of air-sea fluxes for tropical ocean-global atmosphere coupled-ocean atmosphere response experiment. J. Geophys. Res. Oceans 101 (C2), 3747–3764.

Gill, A.E., 1982. Atmosphere-Ocean Dynamics. Academic Press, New York, p. 662.

Haidvogel, D.B., Arango, H., Budgell, W.P., Cornuelle, B.D., Curchitser, E., Di Lorenzo, E., et al., 2008. Ocean forecasting in terrain-following coordinates: Formulation and skill assessment of the regional ocean modeling system. J. Comput. Phys. 227 (7), 3595–3624.

Hill, A.E., Brown, J., Fernand, L., Holt, J., Horsburgh, K.J., Proctor, R., Raine, R., Turrell, W.R., 2008. Thermohaline circulation of shallow tidal seas. Geophys. Res. Lett 35, 1–5. http://dx.doi.org/10.1029/2008GL033459.

Hwang, J.H., Van, S.P., Choi, B.J., Chang, Y.S., Kim, Y.H., 2014. The physical processes in the Yellow Sea. Ocean Coast. Manage. 102, 449–457.

Ichikawa, H., Beardsley, R.C., 2002. The current system in the Yellow and East China seas. J. Oceanogr. 58 (1), 77–92.

IPCC, 2014. Climate change 2014: Impacts, adaption, and vulnerability. Part B: Regional aspects. In: Barros, et al. (Eds.), Contribution of Working Group II to the Fifth Assessment Reoport of the Intergovernmental Panel on Climate Change. Cambridge University Press, Cambridge, United Kingdom and New York, NY, USA, p. 688.

Johnsen, I.A., Fiksen, Ø., Sandvik, A.D., Asplin, L., 2014. Vertical salmon lice behaviour as a response to environmental conditions and its influence on regional dispersion in a fjord system. Aquacult. Environ. Interact. 5, 127–141. http://dx.doi.org/10.3354/aei00098.

Lentz, S.J., 1992. The surface boundary layer in coastal upwelling regions. J. Phys. Oceanogr. 22, 1517–1539.

Li, H., Xiao, T., Ding, T., Lü, R., 2006. Effect of the Yellow Sea cold water mass (YSCWM) on distribution of bacterioplankton. Acta Ecol. Sin. 26 (4), 1012–1019.

Li, H., Yuan, Y., 1992. On the formation and maintenance mechanisms of the cold water mass of the Yellow Sea. Chinese J. Oceanol. Limnol. 10 (2), 97–106.

Li, C.L., Zhai, W.D., 2018. Decomposing monthly declines in subsurface-water pH and aragonite saturation state from spring to autumn in the north Yellow Sea. Cont. Shelf Res.

Liang, X.S., Huang, M., Wu, H., Wang, Y., 2018. The Yellow Sea surface cold patches in warm seasons. In: Liang, X.S., Zhang, Y. (Eds.), Coastal Environment, Disaster, and Infrastructure: A Case Study of China's Coastline. pp. 27–45. http://dx.doi.org/10.5772/intechopen.80732.

Madsen, O.S., 1977. A realistic model of the wind-induced Ekman boundary layer. J. Phys. Oceanogr. 7, 248–255.

Mao, Y., Lin, F., Fang, J., Fang, J., Li, J., Du, M., 2019. Bivalve production in China. In: Smaal, A., Ferreira, J., Grant, J., Petersen, J., Strand, Ø. (Eds.), Goods and Services of Marine Bivalves. Springer.

Pollard, R.T., Rhines, P.B., Thompson, R.O.R.Y, 1973. The deepening of the wind-mixed layer. Geophys. Fluid Dyn. 4, 381–404.

Qi, J., Guo, C., Yang, D., Xu, Z., Yin, B., 2013. 3-D numerical simulation of tidal field near Zhangzi island, NE China. Oceanol. Limnol. Sin. 44 (6), 1469–1478 (in Chinese with English abstract).

Robertson, R., Hartlipp, P., 2017. Surface wind mixing in the regional ocean modeling system (ROMS). Geosci. Lett. 4, 24. http://dx.doi.org/10.1186/s40562-017-0090-7.

Sandvik, A.D., Skagseth, Ø., Skogen, M.D., 2016. Model validation: Issues regarding comparisons of point measurements and high-resolution modeling results. Ocean Model. 106, 68–73. http://dx.doi.org/10.1016/j.ocemod.2016.09.007.

Shchepetkin, A.F., McWilliams, J.C., 2005. The regional oceanic modeling system (ROMS): a split-explicit, free-surface, topography-following-coordinate oceanic model. Ocean Model. 9 (4), 347–404.

Shi, F., Luo, Y., Rong, Z., 2016. A numerical study of the summer circulation in the southwestern Yellow Sea. Acta Oceanol. Sin 35, 1–8. http://dx.doi.org/10.1007/s13131-016-0943-5.

Simpson, J.H., 1981. The shelf-sea fronts: implications of their existence and behaviour. Philos. Trans. R. Soc. Lond. A Math. Phys. Eng. Sci. 302, 531–546.

Simpson, J.H., Hunter, J.R., 1974. Fronts in the Irish Sea. Nature 250, 404–406. http://dx.doi.org/10.1038/250404a0.

Stigebrandt, A., 1985. A model for the seasonal pycnocline in rotating systems with application to the Baltic proper. J. Phys. Oceanogr. 15, 1392–1404.

Su, J., Huang, D., 1995. On the current field associated with the Yellow Sea Cold Water Mass. Oceanol. Limnol. Sin. 26 (suppl.), 1–7.

Sun, Y.J., Cho, Y.K., 2010. Tidal front and its relation to the biological process in coastal water. Ocean Sci. J. 45 (4), 243–251.

Tak, Y.J., Cho, Y.K., Seo, G.H., Choi, B.J., 2016. Evolution of wind-driven flows in the Yellow Sea during winter. J. Geophys. Res. Oceans 121 (3), 1970–1983.

Wang, B., Hirose, N., Kang, B., Takayama, K., 2014. Seasonal migration of the Yellow Sea bottom cold water. J. Geophys. Res. Oceans 119 (7), 4430–4443.

Warner, J.C., Sherwood, C.R., Arango, H.G., Signell, R.P., 2005. Performance of four turbulence closure models implemented using a generic length scale method. Ocean Model. 8 (1–2), 81–113.

Wei, H., Shi, J., Lu, Y., Peng, Y., 2010. Interannual and long-term hydrographic changes in the Yellow Sea during 1977–1998. Deep-Sea Res. II 57 (11–12), 1025–1034.

Wu, X., Cahl, D., Voulgaris, G., 2018. Effects of wind stress and surface cooling on cross-shore exchange. J. Phys. Oceanogr. 48, 2627–2647. http://dx.doi.org/10.1175/JPO-D-17-0216.1.

Xia, C., Qiao, F., Yang, Y., Ma, J., Yuan, Y., 2006. Three-dimensional structure of the summertime circulation in the Yellow Sea from a wave-tide-circulation coupled model. J. Geophys. Res. Oceans 111 (297), http://dx.doi.org/10.1029/2005JC003218.

Xin, M., Ma, D., Wang, B., 2015. Chemicohydrographic characteristics of the Yellow Sea cold water mass. Acta Oceanol. Sin. 34 (6), 5–11.

Xinyou, L., Xiao-Hai, Y., Yuwu, J., Zhenchang, Z., 2016. Performance assessment for an operational ocean model of the Taiwan Strait. Ocean Model. 102, 27–44. http://dx.doi.org/10.1016/j.ocemod.2016.04.006.

Zhao, Y., Zhang, J., Lin, F., Ren, J.S., Sun, K., Liu, Y., et al., 2019. An ecosystem model for estimating shellfish production carrying capacity in bottom culture systems. Ecol. Model. 393, 1–11.

Zhu, J., Shi, J., Guo, X., Gao, H., Yao, X., 2018. Air-sea heat flux control on the Yellow Sea cold water mass intensity and implications for its prediction. Cont. Shelf Res. 152, 14–26.

Zhuang, Y., Liu, Z.Z., Zhai, F.G., 2017. Analysis on continuous current observation in the northern Yellow Sea. Oceanol. Limnol. Sin. 48 (4), 703–711.

Ziegeler, S.B., Dykes, J.D., Shriver, J.F., 2012. Spatial error metrics for oceanographic model verification. J. Atmos. Ocean. Technol. 29, 260–266. http://dx.doi.org/10.1175/JTECH-D-11-00109.1.